Korean J. Chem. Eng., 37(11), 1915-1925 (2020)
DOI: 10.1007/s11814-020-0615-1

pISSN: 0256-1115
eISSN: 1975-7220

Removal of Cr(VI) from aqueous media using magnetic Co-reduced graphene oxide

Nduduzo Nkanyiso Malinga† and Alan Lawrence Leigh Jarvis

Discipline of Electrical, Electronic and Computer Engineering, University of KwaZulu-Natal, Howard College Campus, South Africa

(*Received 21 January 2020 • Revised 26 May 2020 • Accepted 14 June 2020*)

Abstract−The adsorption of Cr(VI) from an aqueous medium using magnetically functionalized cobalt nanoparticles-reduced graphene oxide (Co-rGO) was studied. Co-rGO was synthesized using the co-precipitation method. Graphene oxide and cobalt acetylacetonate were reduced together in water using sodium borohydride as a reducing agent. Co-rGO was used as the adsorbent material for the removal of dichromate ions in water. The prepared Co-rGO was characterized using powder X-ray diffraction (XRD), Transmission electron microscopy (TEM), and Brunauer-Emmett-Teller (BET) surface area analysis. Selected area electron diffraction was used to determine that the cobalt nanoparticles were on the surface of the reduced graphene oxide. The effect of the mass of the adsorbent material (Co-rGO), the concentration and pH of the Cr(VI) containing solution and the time of contact between the adsorbent and the Cr(VI) on the adsorption efficiency were investigated. It was found that the optimum adsorbent mass for the efficient removal of Cr(VI) from a fixed concentration of Cr(VI) of 100 mg L^{-1} was 0.015 g, the optimum pH of the solution was 8, and the optimum contact time was 90 minutes. The experimental data obtained were fitted to the Langmuir, Freundlich, and Lui isotherms to obtain the characteristic parameters of each model. The experimental data fitted well to the Freundlich isotherm. The thermodynamic data was used to evaluate the nature of the adsorption. It was determined that the sorption process was physisorption. The kinetics of the adsorption process followed pseudo-second-order kinetic model.

Keywords: Magnetic Properties, Adsorption, Magnetic Nanoparticles, Cr(VI), Cobalt Nanoparticles

INTRODUCTION

Chromium is widely used in several different industrial applications, such as metallurgy, electroplating, pigments and wood preservation [1-3]. The trivalent chromium (Cr(III)) ions are a micronutrient in biological systems, which play a pivotal role in glucose levels normalization, metabolism of lipids and steroid regulation. Cr(VI) is a largely toxic carcinogen, being in the hexavalent state it serves as a strong oxidizing agent to return to trivalent state. In living cells hexavalent chromium forms free radicals in the form of reactive oxygen species, which damages DNA and causes oxidative stress in cellular activities [4]. The hexavalent chromium is introduced to water systems by human industrial activity. This is catastrophic to environmental systems as it kills flora and fauna. Most plants do not have a proper and specific transport system for chromium. It interferes with the carrier channels for essential micronutrients, which in turn alters the germination process, photosynthesis and other metabolic pathways [4]. Cr(VI) is highly toxic to humans. Cr(VI) is a hindrance to human health because it blocks metalloenzymes systems which carry out metabolic functions including mitochondrial function [5]. Other effects of Cr(VI) poison are on the liver and kidney through ingestion of contaminated water or food [5]. Cr(VI) is also a carcinogenic agent which alters the DNA transcription process [6]. The environmental protection agency (EPA) of the United States has recognized Cr(VI) compounds as a top priority toxin. Thus, there is a need for an economical method of remediation to remove Cr(VI) from fresh water.

Most reported methods of remediation of Cr(VI) include ion exchange, coagulation, precipitation, adsorption and membrane filtration [7-13]. Adsorption has been categorized as an economical method when compared to the other methods. One of the contenders for adsorption is activated carbon, which has some problems such as fouling. The discovery of carbon nanotubes and graphene has allowed the expansion of the adsorption of Cr(VI) technology. These materials have been reported to have high surface area, which in turn has a large number active for the adsorption of Cr(VI). Graphene is obtained from the reduction of graphene oxide, which is a single graphite oxide sheet [14]. Graphene oxide contains oxygenated functional groups such as hydroxyl, epoxide, carbonyl and carboxyl groups. Graphene has generally slow adsorption kinetics of Cr(VI). Nanoparticles have been studied to remove Cr(VI) from aqueous solution. Nanoparticles have a high surface-to-volume ratio, which has been shown to have benefits of fast adsorption kinetics. Magnetic nanoparticles usually have poor adsorption capacity for Cr(VI) because of the agglomeration of the nanoparticles [15]. The combination of nanoparticles with reduced graphene oxide improves the dispersion of the nanoparticles. The adsorption of Cr(VI) on reduced graphene oxide decorated with magnetic nanoparticles occurs via electrostatic interaction [16]. The nanoparticles Fe_2O_3 are ferromagnetic, which allows the formed Fe_2O_3 reduced graphene oxide nanocomposite (Fe_2O_3-rGO) to be easily removed using a hand held magnet. The ease of separation allows the nanocomposite to be reusable. Fe_2O_3-rGO with the adsorbed Cr(VI) is ultra-sonicated in a solution of pH 9 to remove the adsorbed Cr(VI) from

†To whom correspondence should be addressed.
E-mail: 205500488@stu.ukzn.ac.za

Fe_2O_3-rGO [15]. In this study, cobalt nanoparticles on reduced graphene oxide nanocomposite (Co-rGO) were used in the removal of Cr(VI) from aqueous solution. Cobalt nanoparticles are superparamagnetic and when conjugated with reduced graphene oxide, the composite becomes a weak ferromagnetic substance. The composite can be easily attracted to a handheld magnet. It also has a high surface area which can be applied in the adsorption of pollutants in aqueous media. Cobalt nanoparticles are well dispersed in the matrix of the reduced graphene oxide. This ensures a large number of active sites for adsorption of Cr(VI), which makes the Co-rGO an effective adsorbent for Cr(VI). The ferromagnetic nature of the Co-rGO allows the adsorbent material to easily separate from samples containing Cr(VI) ions. Cr-rGO was selected as a mono metallic and non-metal oxide nanoparticles graphene composite to be used in the removal of Cr(VI) ions. It was reported before on Ni-rGO composite; however, it catalyzed the reduction of Cr(VI) to Cr(III). In the case of this experiment, the emphasis is on the removal of the Cr(VI). The Co-rGO is the first monometallic nanoparticles graphene which was used for removal of Cr(VI) from aqueous media. The Co-rGO was characterized using XRD, TEM, Raman and IR. The ability of Co-rGO as sorbent material for Cr(VI) was evaluated in basic media. The removal efficiency of the Co-rGO was evaluated and the kinetics of the adsorption was also evaluated.

EXPERIMENTAL

1. Materials

Phosphoric acid 85% (H_3PO_4), sulfuric acid 98% (H_2SO_4), potassium permanganate ($KMnO_4$) 99%, sodium hydroxide 99% (NaOH), ethanol 99.9% and hydrochloric acid (HCl) 35% were purchased from Associated Chemical Enterprise. Cobalt acetylacetonate 98% (Co acac) and potassium dichromate ($K_2Cr_2O_7$) were purchased from BDH Chemicals. Trisodium citrate and sodium borohydride were purchased from Sigma Aldrich. Expandable graphite grade KP9950200 was donated by Richards Bay minerals.

2. Equipment

Infra-red (IR) spectra were recorded on a Perkin-Elmer Spectrum 100 ATR FT-IR spectrometer. X-ray powder diffraction (XRD) patterns were recorded on a PAN analytical, EMPYREAN, using a Co-Kα monochromatic radiation with PIXcel detector. Data were collected in the range from 2θ=5° to 90°, scanning at 2° min^{-1} with a filter time-constant of 2.5 s per step and a slit width of 6.0 mm. Transmission electron microscope (TEM) images were recorded on a JEOL JEM 1010 with the accelerating voltage of 18 kV. Thermogravimetric analysis (TGA) together with differential scanning calorimetry (DSC) was recorded on Q600 SDT TA Instruments. The samples were placed in ceramic pan and measurements conducted under nitrogen flow (20 mL min^{-1}) from room temperature to 1,000 °C at a heating rate of 10 °C min^{-1}. Magnetization experiments were recorded on the Lakeshore Vibrating Magnetometer System 735S, with an external applied magnetic field of −15 kOe to 15 kOe. UV/Vis spectra were recorded using a Perkin Elmer Lambda 25 UV/Vis spectrophotometer. Inductively coupled plasma-optical emission spectroscopy (ICP-OES), Perkin Elmer Optima 5300 DV. WinLab 32 software was used to analyze the data. Ultrasonication was done using an ultrasonic bath, Digital Ultrasonic Cleaner PS 100 A with a frequency of 40 kHZ, time interval of 30 minutes and a power of 600 W. Exfoliation of expendable graphite was done using a Defy MDM 03617, with a power of 700 W.

3. Method

3-1. Synthesis of Graphene Oxide (GO)

Graphene oxide was synthesized according to method outlined in literature [17].

Expandable graphite (3.11 g) was exfoliated in a microwave oven for 30 seconds yielding expanded graphite. The graphite was then mixed with phosphoric acid (30 mL) into 30 mL pill vial. The pill vial was sealed and placed in an ultrasonic bath and ultrasonicated for 1 hr. The graphite was dispersed in the acid and was transferred to 500 mL round bottom flask. The flask was cooled to 0 °C and sulfuric acid (270 mL) was added dropwise. The solution was stirred, followed by the slow addition of potassium permanganate (13.5 g). The solution was stirred for 12 hrs and then cooled to room temperature followed by the addition of ice (400 mL) and H_2O_2 (3 mL). The mixture was sifted through a metal sieve with the filtrate collected. The filtrate was the centrifuged to collect the solid product, which was washed with water, HCl and ethanol.

3-2. Synthesis of Graphene Decorated with Cobalt Nanoparticles (Co-rGO)

The reduced graphene oxide-cobalt nanoparticle composite was synthesized based on reported methods [18,19]. Graphene oxide (1.01 g) was mixed with 25 ml deionized water and ultrasound until the graphene oxide was well dispersed and formed a dark brown solution. The solution was transferred into 250 mL 3-neck volumetric flask. Cobalt acetylacetonate (Co acac) (2 g) and potassium hydroxide (0.05 g) were weighed into the solution and refluxed at 90 °C for 2 hours. After 2 hours had passed, sodium borohydride 0.6 M (10 mL) solution was added to the reflux solution dropwise followed by the addition of solution of trisodium citrate 0.1 M (10 mL) and refluxed for 2 hours at 90 °C. The solution was centrifuged and the supernatant was decanted away. The remaining solid was washed with copious amounts of hot water (60 °C) and ethanol. The solid was dried under vacuum at 40 °C.

4. Adsorption Experiments

The adsorption experiments were contained in a series of Erlenmeyer flasks containing 50 mL solution of Cr(VI) ions. The adsorption tests were conducted to evaluate the uptake of the Cr(IV) ions by Co-rGO. Different parameters, such as mass of adsorbent, initial concentration, pH, and contact time, were evaluated. The Cr(VI) solutions were fashioned from 1,000 mg L^{-1} standard solution. A working amount of 100 mg L^{-1} was used to create samples ranging from 10 to 80 mg L^{-1}. The mass of the Co-rGO used as an adsorbent was varied from 3 mg to 25 mg to determine the optimal for the mass for the adsorption of Cr(VI). The pH of the Cr(VI) solutions ranged from 2 to 12, were adjusted using 0.1 M HCl and 0.1 NaOH. The agitation time was varied from 30 to 180 minutes. The temperature of Cr(VI) varied from 298 to 318 K. The Co-rGO was separated from the Cr(VI) solution with the aid of rare-earth magnet. The supernatant was collected, and the remaining heavy metal ion was evaluated using ICP-OES. The removal efficiency (R, %) and the amounts of heavy metal ions adsorbed q (mg/g) were determined according to the formula:

$$R = \frac{(C_0 - C_t)}{C_0} \times 100\%, \quad (1)$$

$$q = \frac{(C_0 - C_e)V}{m}, \quad (2)$$

where R is the removal efficiency of the metals ions, C_0 (mg L^{-1}) is the initial concentration of metal ion, and C_t (mg L^{-1}) is the concentration of metal ion at time (t), q (mg g^{-1}) is the amount of metal ion adsorbed per unit amount of adsorbents, V (L) is the volume of adsorbates, m (g) is the mass of the adsorbents.

5. Kinetics and Adsorption Studies

The kinetics of the adsorption was calculated using pseudo-first order rate Eq. (3) [20], second-order rate Eq. (4) [20] and Avrami Eq. (5) [21], which are shown below:

$$q_t = q_e(1 - e^{-k_1 t}), \quad (3)$$

$$\frac{t}{q_t} = \frac{1}{k_2 q_e^2} + \frac{t}{q_e}, \quad (4)$$

$$q_t = q_e[(1 - e^{-k_3 t})]^{n_A}, \quad (5)$$

where k_1 (min^{-1}) is the rate constant for the pseudo-first-order rate equation, k_2 is the rate constant for pseudo-second-order rate equation, k_3 is the Avrami rate constant and n_A is the Avrami constant. q_e (mg g^{-1}) and q_t (mg g^{-1}) are the amounts of Cr(VI) adsorbed at equilibrium and at time (t), respectively.

The adsorption isotherms also relate the amount of the chromate ions adsorbed at equilibrium, as per weight of the adsorbent, q_e (mg g^{-1}) to the adsorbate concentration also at equilibrium, C_e (mg L^{-1}). The data was evaluated using three isotherms equations: Langmuir, Freundlich and Lui. The Langmuir model [22], Freundlich [24] and Liu model/equations are given below.

Langmuir:

$$q_e = \frac{bq_m C_e}{1 + bC_e}, \quad (6)$$

where q_m (mg g^{-1}) and b are Langmuir constants related to the adsorption capacity and the energy of the adsorption.

Freundlich:

$$q_e = K_F C_e^{1/n}, \quad (7)$$

where K_F is the adsorption capacity and n is the adsorption intensity.

Lui:

$$q_e = \frac{q_m (K_L C_e)^{n_L}}{1 + (K_L C_e)^{n_L}}. \quad (8)$$

where K_L, is the adsorption capacity, C_e is equilibrium concentration and n_L is the dimensionless exponent of the Lui equation. The statistical evaluation of the data was obtained using determination coefficient R^2 and standard deviation SD.

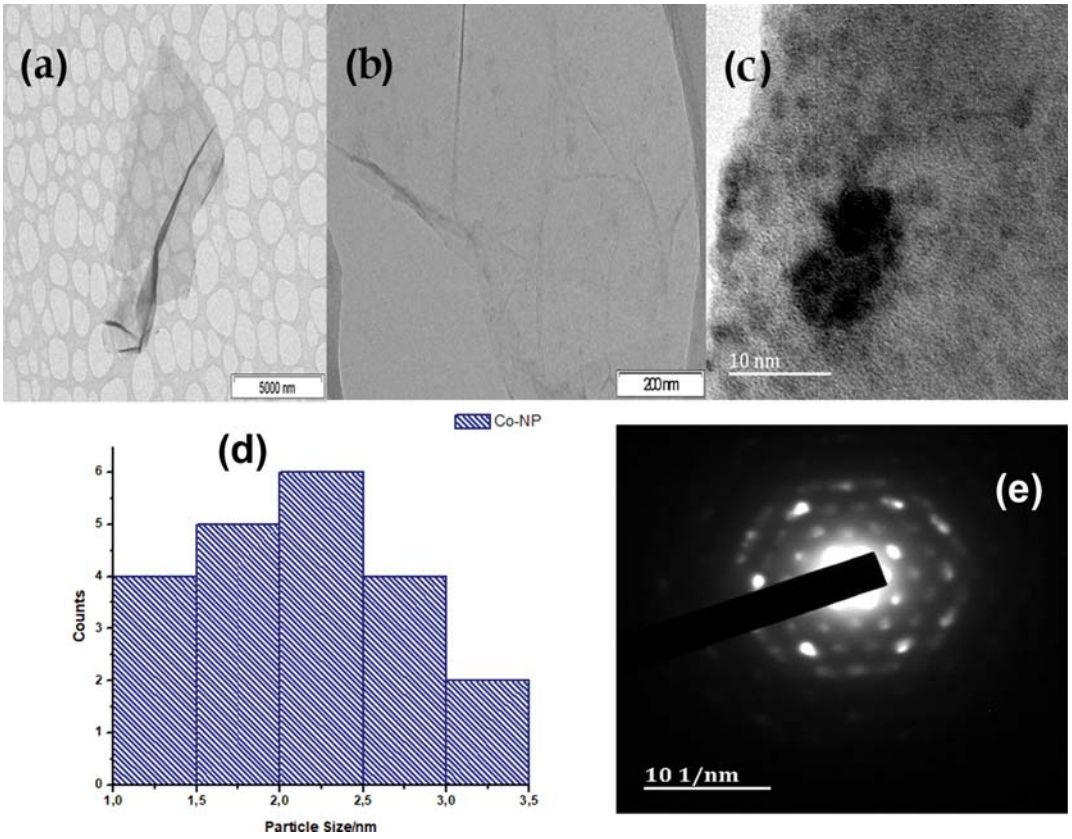

Fig. 1. TEM images of (a) GO, (b) rGO and (c) Co-rGO, (d) Particle size distribution of Co-NP on graphene and (e) SEAD spectrum of Co-rGO.

RESULTS AND DISCUSSION

1. Synthesis and Characterization

The study proceeds with the synthesis of intermediate graphene oxide which was used subsequently in the synthesis of sample of interest Co-rGO. The TEM image of GO is shown in Fig. 1(a). The GO is monolayered and slightly wrinkled. The reduced graphene oxide is shown in Fig. 1(b), which was obtained from the reduction of graphene oxide using sodium borohydride. The Co-rGO was synthesized from the coprecipitation method and the synthesis success was verified using TEM, seen in Fig. 1(c). Fig. 1(c) shows the cobalt nanoparticles, which are the dark spots in the graphene matrix. The nanoparticles were slightly agglomerated and were small. Image J software was used to evaluate the particle size distribution of the cobalt nanoparticles. It was found that the average particle size was between 1.32 nm to 3.25 nm and the average particle size was 1.89 nm with a standard deviation of ±0.531. A graph of the particle size distribution is shown in Fig. 1(d). The selected area electron diffraction (SAED) is shown in Fig. 1(e). The spectrum has spots which show that the Co-rGO sample was monocrystalline [25]. The ICP-OES was used for both qualitative and quantitative analysis for the verification of cobalt nanoparticles conjugation. The amount of cobalt conjugated to reduced graphene oxide was determined using ICP-OES which was found to be 15 mg g^{-1}.

Infrared spectra with characteristic absorption frequencies of the specimens are shown in Fig. 2. The FTIR spectrum for GO has strong absorption for carboxylic acid (O-H) 3,263 cm^{-1}, carbonyl (C=O) 1,624 cm^{-1} and alkoxy (C-O) 1,042 cm^{-1} [26]. In contrast the FTIR spectra for rGO and Co-rGO, the bands for the oxygenated carbon have diminished. However, there is a peak at 2,100 cm^{-1} attributed to =C-H aliphatic [28]. It is observed that a significant quantity of oxygenated groups was lost during the reduction with sodium borohydride. The Co-rGO spectrum has absorption at 813 cm^{-1} which was for Co-O band [27]. Raman spectra, shown in Fig. 3, wer in the range of 500 cm^{-1} to 3,400 cm^{-1}. The characteristic band graphitic material is *D*-band (1,346 cm^{-1}), *G*-band (1,580 cm^{-1}) and 2*D*-band (2,720 cm^{-1}). The peak at 1,000 cm^{-1} is attributed to the silicon wafer sample holder [29,30]. The spectrum of the Co-rGO had a slight red shift in the D and G bands. The D-band is used to determine the level of disorder, imperfection and impurities in graphene. While the G-band corresponds to the vibration of sp^2 hybridized carbon bonded atoms in the graphene lattice [31]. The ratios of ID/IG in both the spectra were greater than 1, showing the defects and disorder in the graphene structure, which is common in graphene material obtained by the chemical reduction method. The 2D peak is broad and wide, which is an indication that the rGO and Co-rGO are multilayered. It has been reported that the shape and width of 2D peak are used to determine the number of layers of graphene [31]. A sharp peak indicates a mono-

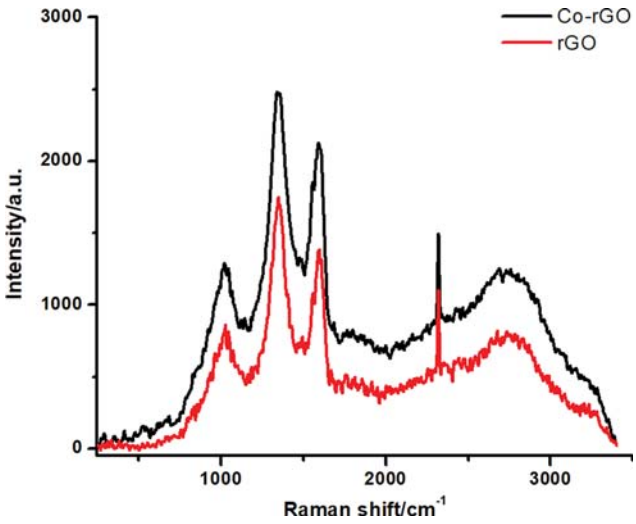

Fig. 3. Raman spectra of Co-RGO and rGO.

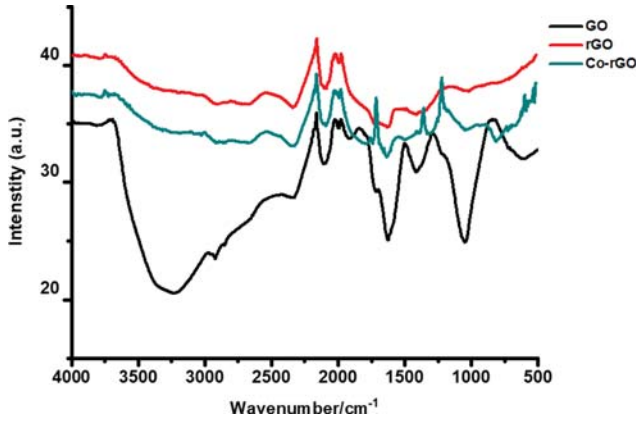

Fig. 2. Infra red spectra of GO, rGO and Co-rGO.

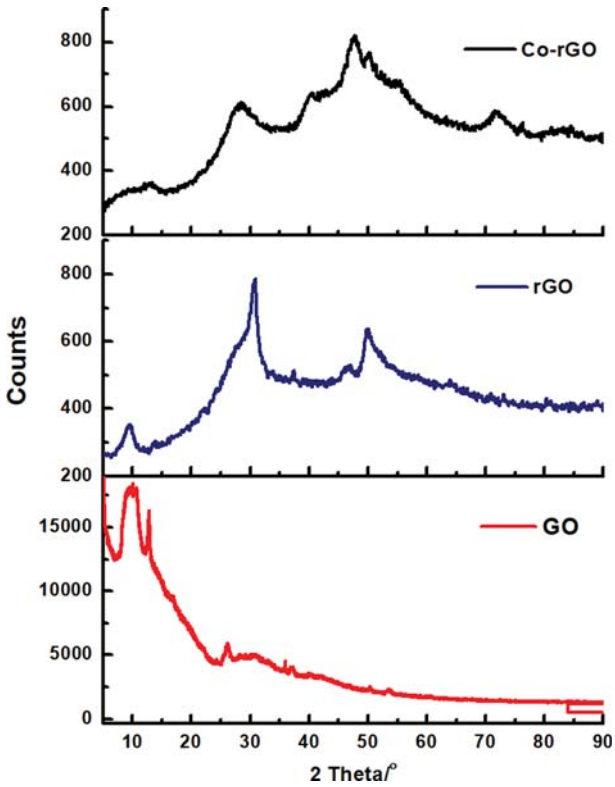

Fig. 4. XRD spectra of GO, rGO and Co-rGO.

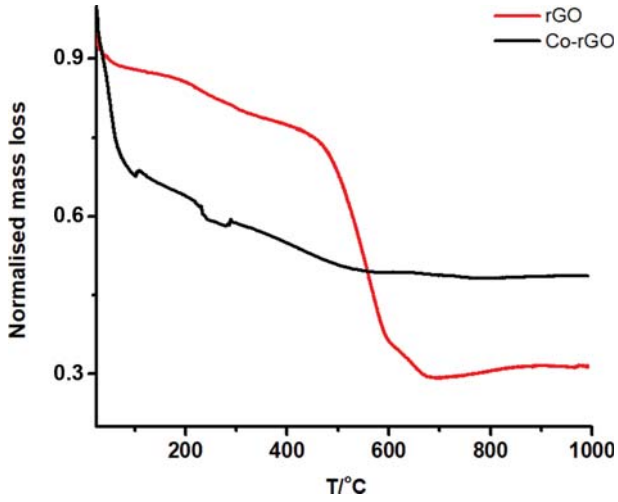

Fig. 5. Thermograms of rGO and Co-rGO from TGA.

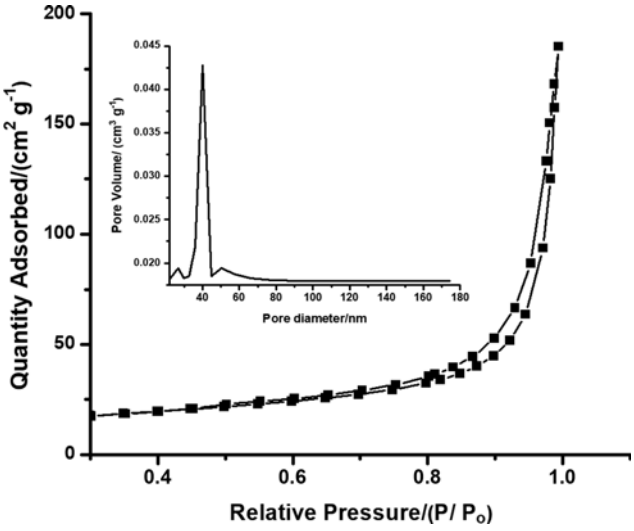

Fig. 6. BET analysis of Co-rGO.

layer graphene, while a broad peak indicates a multi-layer graphene [31].

XRD spectra of the prepared samples are shown in Fig. 4. The XRD pattern for graphene oxide shows a characteristic peak at 10° for graphene oxide. The peak is broad and prominent, easily dwarfing other peaks. The broadness of the peak is indicating that the graphene oxide is amorphous. The XRD pattern for rGO and Co-rGO has a peak at 26° which is due to graphene [18]. The peaks associated with cobalt nanoparticles are 47° and 77° [18]. The thermal stability of Co-rGO was investigated using thermogravimetric analysis and shown in Fig. 5. The Co-rGO specimen had a multi-step degradation pattern which is due to water loss. The other mass loss was due to oxygenated carbon material present both in the capping agent of nanoparticles and reduced graphene oxide [25,32]. The Co-rGO surface area was determined using adsorption and desorption of nitrogen gas using BET model shown in Fig. 6. The specific surface area was determined to be 92 m^2 g^{-1}. The Barret-Joyner-Halenda (BJH) analysis was used to determine the pore volume of the Co-rGO. The pore volume was found to be 0.0284 cm^3 g^{-1} with a pore diameter of 4.5 nm. The magnetic response of the specimens was determined with a vibrating sample magnetometer (VSM). The specimens were vibrated in the presence of sweeping electromagnetic field from −15 kOe to 15 kOe and shown in Fig. 7. The cobalt nanoparticles are superparamagnetic behavior, which is characterized by small coercivity. The formation of the graphene nanocomposite had decreased the saturation magnetization. The electronic interaction between the nanoparticles and the rGO changes magnetic anisotropy, which in turn increases the coercivity and loss of superparamagnetism to ferromagnetic behavior [33]. The Co-rGO has a quenched magnetic response when compared to that of cobalt nanoparticles. The saturation magnetization

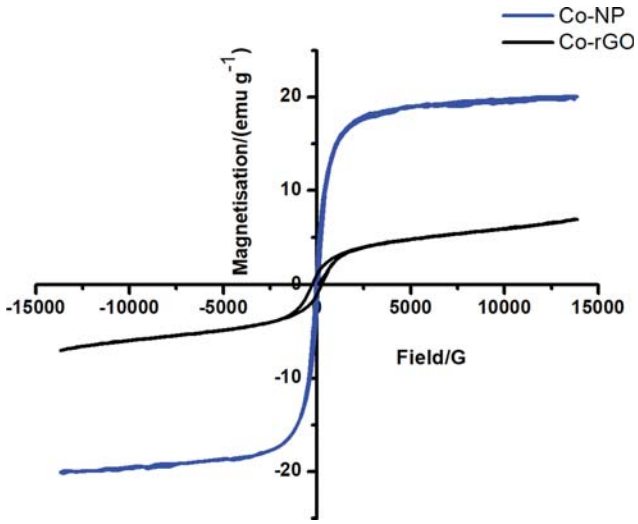

Fig. 7. Hysteresis loops of Co-NP and Co-rGO.

of cobalt nanoparticles was 20.1 emu g^{-1}. The specimen magnetization response of Co-rGO was 6.8 emu g^{-1}. Both the specimens have low coercivity as seen in Table 1, suggesting that the specimens are a soft magnetic material [27].

2. Removal of Cr(VI) in Water

The removal of the chromate ions in water is shown in Fig. 8. The figure shows (a) Cr(VI) solution before removal, (b) Cr(VI) solution with Co-rGO before three hours had lapsed and (c) Cr(VI) solution with Co-rGO after three hours had lapsed. It was observed that the magnet attracted Co-rGO from the solution, as shown in Fig. 8(c). The color of the solution also changed from a dark yel-

Table 1. Saturation magnetization (M_s), maximum magnetization (M_m), remanent magnetization (M_r) and coercive fields (H_c)

Specimen	M_s (emu g^{-1})	M_m (emu g^{-1})	M_r (emu g^{-1})	H_c (Oe)
Co-NP	20.1	20.1	20.1	67.7
Co-rGO	6.81	7.01	6.95	273.1

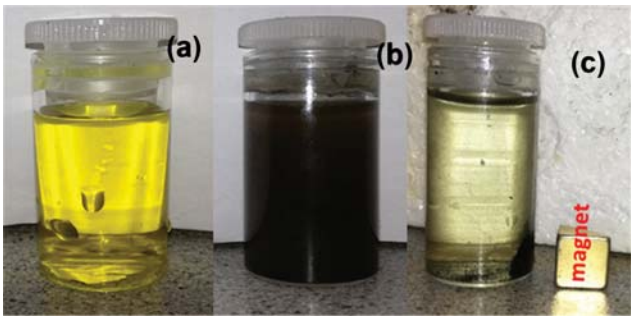

Fig. 8. Photograph showing removal of chromate ions in water using Co-rGO, (a) chromate solution, (b) chromate solution with Co-rGO and (c) solution of Cr (VI) after adsorption of Cr(VI) ions.

low shown in Fig. 8(a), which showed the presence of Cr(VI) ions to a pale/faint yellow as observe in the Fig. 8(c), after the removal of Cr(VI) ions by the Co-rGO.

The effect of Co-rGO dosage on the removal efficiencies of Cr(VI) was evaluated and shown in Fig. 9(a). The concentration of Cr(VI) ions used in this study was 100 mg L^{-1}. The temperature of the Cr(VI) solution was kept at 298 K and the agitation time was 3 hrs. The dosages of Co-rGO were 80, 100, 160, 200, 300 and 400 mg L^{-1}. The results showed that the adsorption efficiency of Co-rGO increased with increasing dosage of Co-rGO and started to plateau at 65% removal efficiency as shown in the Fig. 9(a). The dosages of 80, 100, 160 and 200 mg L^{-1} had removal efficiencies of 15, 23, 37 and 43%. The pH of the solution is as an important parameter in controlling the adsorption process [34]. The effect of pH on the removal efficiency of Cr(VI) was evaluated and the results are shown in Fig. 9(b). The pH of the Cr(VI) solution was in the range of 2 to 12. It was observed that at low pH the removal efficiency was low; the increase in pH saw a rise in the removal efficiency. The results showed at pH of 8 had the highest removal efficiency, which was 40%. Further increase in the pH beyond 8 saw a decrease in the adsorption efficiency. In basic media the Cr(VI) exists as CrO_4^{2-}, which has an affinity for the Co-rGO, which is positively charged [35,36]. At pH greater 8 there is a high concentration of OH^- that competes for adsorption with Cr(VI) ions, as reported previously [37,38]. The graphene nanocomposites with metallic oxide nanoparticles remove Cr(VI) efficiently at lower pH because metallic oxides have an affinity for H^+ ions [38]. The effect of initial concentration of the Cr(VI) ions was evaluated. The ob-

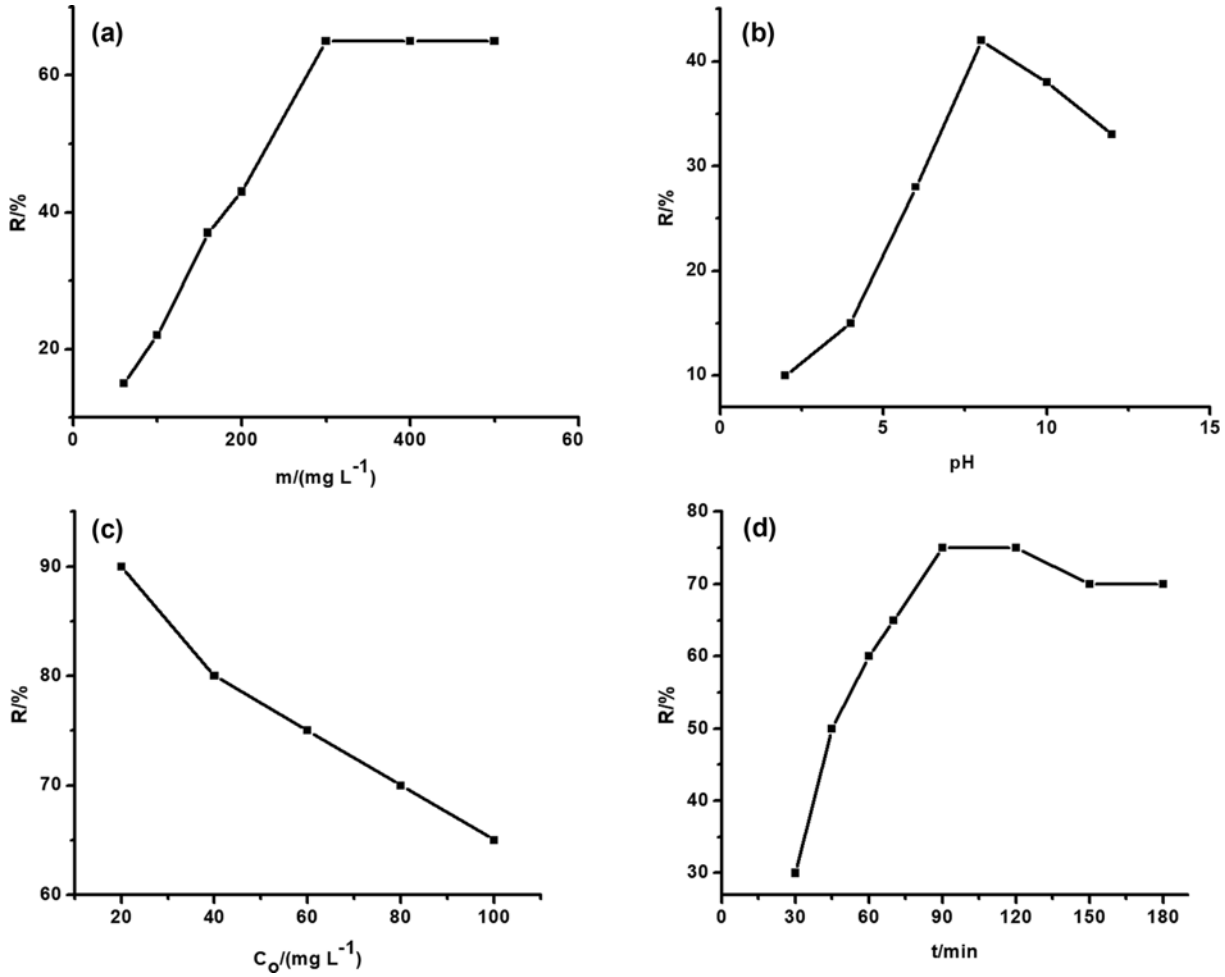

Fig. 9. Effect of initial parameters such (a) dosage, (b) pH, (c) concentration and (d) contact time on removal efficiency of Cr(VI).

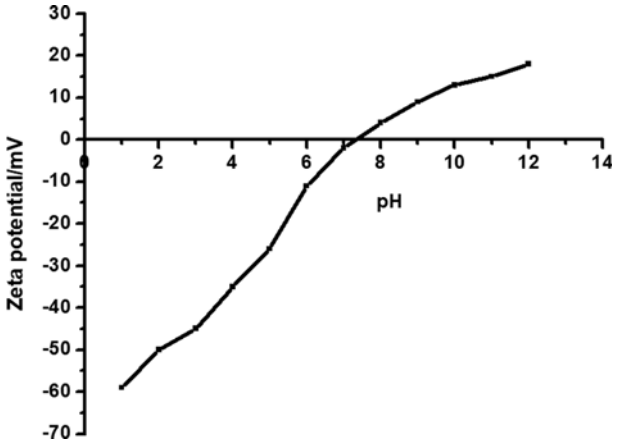

Fig. 10. Point zero charge of Co-rGO.

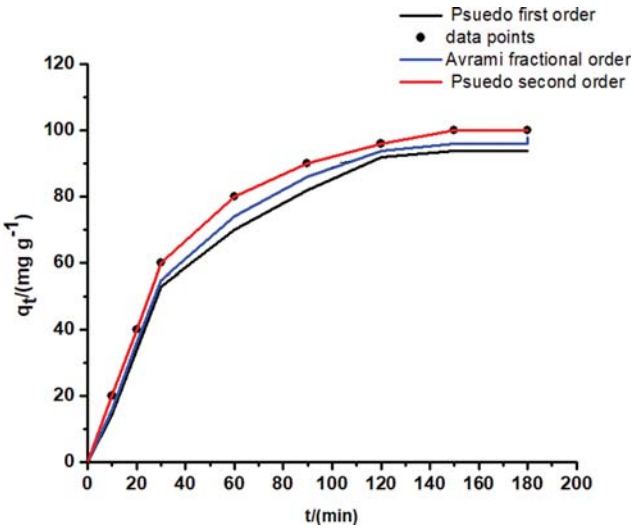

Fig. 12. Adsorption kinetics curves of the Cr(VI) on the Co-rGO.

tained data, shown in Fig. 9(c), shows the initial concentration of Cr(VI) with the highest removal efficiency was 20 mg L^{-1}. The removal efficiency decreased with increasing concentration of Cr(VI). This trend was expected because the increase in concentration tends to saturate active sites, which in turn lowers the removal efficiency [39]. The effect of contact time is shown in Fig. 9(d). The removal of the heavy metal Cr(VI) ions reached equilibrium at 90 min. The point zero charge was determined according to the reported method [40]. The potential was measured as a function of the changing pH and shown in Fig. 10. The results show that the surface charge above the pH of 7.35 is positive. The operating pH of Co-rGO in this experiment was 8, which was positively charged and will attract the negatively charged CrO_4^{2-} ions. The proposed mechanism shown in Fig. 11 is that the cobalt nanoparticles.

3. Adsorption Studies

3-1. Adsorption Kinetics

The adsorption parameters and the kinetics of the adsorption process are important parameters to evaluate. This is important in dealing with wastewater purification. The parameters determined in the above section were used in this study, which were the concentration or 20 mg L^{-1}, pH of 8 and contact time of 90 min. The adsorption kinetics was evaluated pseudo-first-order, pseudo-sec-

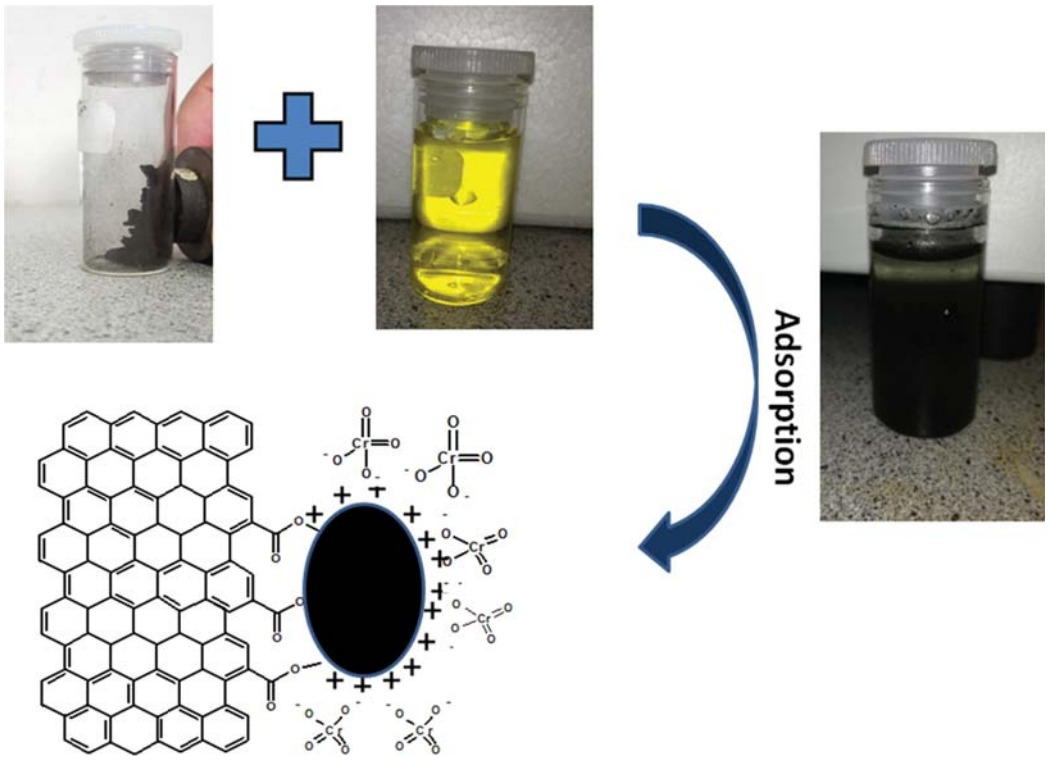

Fig. 11. Proposed scheme of the adsorption Cr(VI) ions on Co-rGO.

Table 2. Table of constants and correlation coefficient

Pseudo-first-order				Pseudo-second-order				Avrami fractional order			
$k_1/(min^{-1})$	$q_e/(mg\ g^{-1})$	R^2	SD	$k_2/(g\ mg^{-1}\ min^{-1})$	$q_e/(mg\ g^{-1})$	R^2	SD	$k_1/(min^{-1})$	$q_e/(mg\ g^{-1})$	R^2	SD
0.0319	89.9	0.945	20.7	0.0421	92.3	0.992	4.33	0.0347	90.6	0.981	7.89

ond-order kinetic models and Avrami fraction kinetic model [22, 41]. The data was plotted as Fig. 12 and summarized in Table 2. From the plotted data it is observed that the adsorption of Cr(VI) on Co-rGO, follows a pseudo-second-order kinetics model. This was evaluated using the statistical R^2 values of the data. The correlation coefficient the pseudo-second-order was 0.992, which was closer to 1. R^2 was to evaluate the how the model correlated to the obtained values. The pseudo-second kinetic equation had the highest R^2 when compared to the other two models. It also had the lowest standard deviation value of 4.33, which indicated that the adsorption kinetics followed the pseudo-second-order kinetic equation. The Avrami fractional order kinetic model and the pseudo-first-order kinetic model had R^2 values of 0.981 and 0.945. The correlation coefficient has been used as a measure of good fit of experimental data on the kinetic model. The pseudo-first-order kinetic model had the highest standard deviation of about 20.7. The calculated value for q_e was determined from the graph: 92.3 mg g^{-1}.

3-2. Adsorption Isotherms and Thermodynamics Parameters

The adsorption isotherm was used to determine the distribution of the chromate molecule within the solid phase when the adsorption process reaches equilibrium [28]. The adsorption isotherms also relate the amount of the chromate ions adsorbed at equilibrium, as per weight of the adsorbent, q_e (mg g^{-1}) to the adsorbate concentration also at equilibrium, C_e (mg L^{-1}). The extent of how well the experimental data fitted to the studies models was evaluated using R^2 and SD values. Values of R^2 and SD which are closer to 1 denote that the data fitted the model better. It also affirms that there are no differences between the experimental and theoretical values. The raw data was plotted in Fig. 13.

The data was summarized in Table 3. The Langmuir isotherm describes an adsorption process which is monolayered has uniform distribution process between the adsorbed. This correlated to the adsorbed molecules having no interaction with each other and the adsorption surfaces were of equivalent energies. However, it was determined that the R_L was less than 1, which meant that the adsorption process was unfavorable [41]. The Freundlich isotherm describes a monolayered to multilayered adsorption of heterogeneous surfaces. The adsorption is between the liquid and solid surfaces. The model assumes that there is interaction between the adsorbed molecules [42-45]. The nature of the adsorption can be verified by the value of n_F. If n_F=1, the adsorption is chemical, when n_F<1 the adsorption is unfavorable, and n_F>1 is favorable. The data fitted well to the Freundlich isotherm and the value n_F was 2.99 at 298 K. This affirms that the adsorption fitted well to the Freundlich isotherm and that the process was favorable. The correlation coefficient R^2 was 0.996. This was closer to 1 and standard deviation for the Freundlich fitting was the lowest and the adsorption could be multilayered. There was a decrease in the adsorption capacity when the temperature which was expected since it is

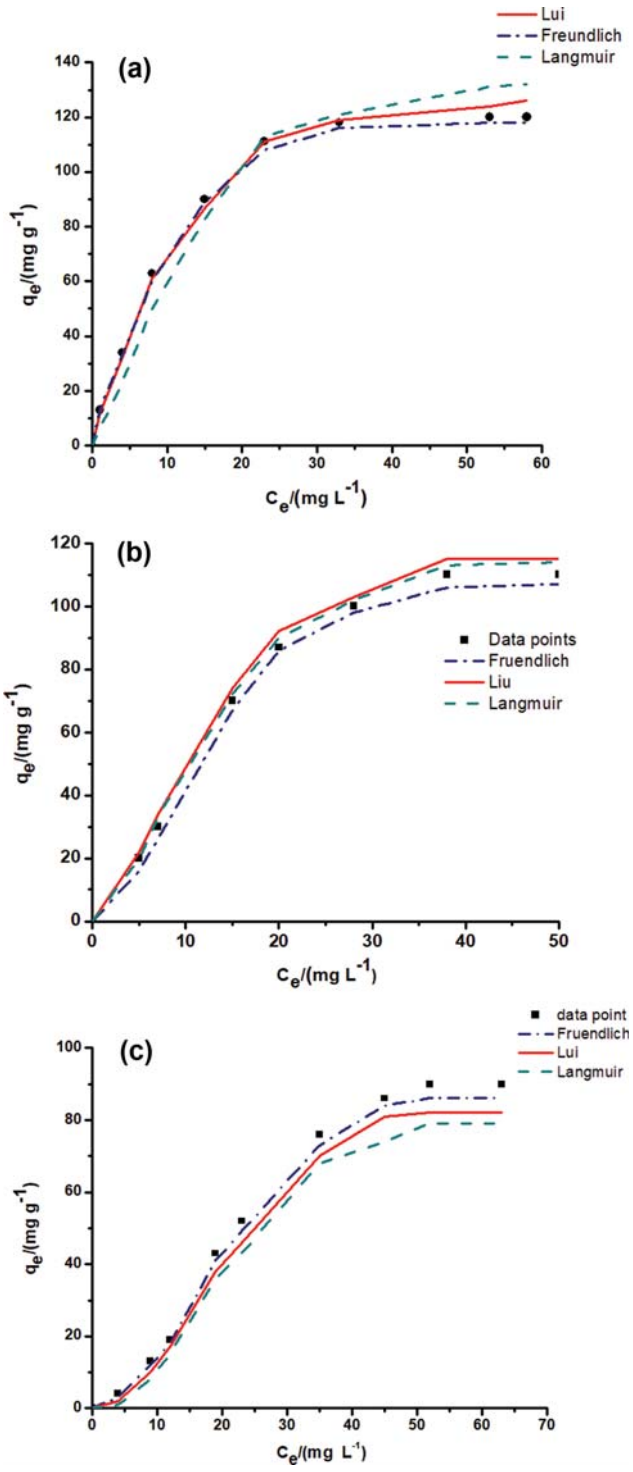

Fig. 13. Adsorption isotherms (Langmuir, Freundlich and Lui) Cr(VI) on Co-rGO at different temperatures (a) 298 K, (b) 308 K and (c) 318 K.

Table 3. Table of constant and adsorption isotherms

T/K	Langmuir					Freundlich				Lui				
	q_m (mg g^{-1})	b (L mg^{-1})	R_L	R^2	SD	K_F	n_F	R^2	SD	K_L (L g^{-1})	Q_m (mgg^{-1})	n_L	R^2	SD
298	113.3	0.689	0.456	0.989	3.29	17.1	2.99	0.996	0.632	0.119	119.5	1.21	0.969	5.77
308	106.2	0.519	0.325	0.948	5.51	12.3	2.22	0.989	0.741	0.418	108.4	1.15	0.926	2.97
318	82.3	0.332	0.192	0.922	3.62	10.3	2.05	0.945	0.845	0.621	88.8	1.13	0.882	3.87

Table 4. Maximum adsorption capacity for the adsorption of (VI) on carbon based materials

Adsorbent	Adsorbate	Adsorption capacity/(mg g^{-1})	Conditions	References
Co_3O_4-rGO	Cr(VI)	208.8	298 K, pH=2	[32]
GSC	Cr(VI)	2,859.4	298 K, pH=1.5	[14]
ZVI-Fe_3O_4-rGO	Cr(VI)	101	298 K, pH=8	[32]
rGO	Cr(VI)	98.2	298 K, pH=2	[27]
MWCNT-Fe_3O_4	Cr(VI)	65	298 K, pH=3	[40]
Activated carbon	Cr(VI)	69	298 K, pH=3	[41]
Magnetic rGO-loaded PEGDMA	Cr(VI)	119	298 K, pH=3	[15]
Co-rGO	Cr(VI)	116.8	298 K, pH=8	This work

well reported in literature [42-46]. The increase in the temperature corresponds to the decrease adsorption capacity the Co-rGO. The comparison of obtained adsorption capacity compared to other carbon based materials is summarized in Table 4.

The thermodynamic equilibrium constant can be determined using the following equations [21,22]:

$$K_d = \frac{q_e}{C_e} \tag{9}$$

$$\Delta G = -RT\ln K_d \tag{10}$$

$$\ln K_d = \frac{\Delta S}{R} - \frac{\Delta H}{RT} \tag{11}$$

where R (8.314 J mol^{-1} K^{-1}) is the gas constant, T (K) is the absolute temperature, K_d is the thermodynamic equilibrium constant, ΔG (kJ mol^{-1}) is the Gibbs free energy, ΔH (kJ mol^{-1}) is enthalpy of the adsorption and ΔS (J mol^{-1} K^{-1}) is entropy. The ΔH and ΔS are calculated by plotting the van't Hoff equation in the form of $\ln K_d$ vs 1/T and are shown in Fig. 14. From Table 5, the Gibbs energy values were negative, suggesting that the adsorption is spontaneous. The positive value of the entropy suggests there is a high disorder in the system and increased randomness. The interaction between the solution and solid is increased. The interface solid/solution had an increased uptake of Cr(VI) by the Co-rGO. Thus the Co-rGO has an affinity for Cr(VI) ions. The enthalpy of the sorption process was negative, which affirms the process is exothermic [20,21]. The magnitude of the enthalpy can be used to distinguish between chemisorption and physisorption. For ΔH>40 kJ mol^{-1} the sorption process is a chemisorption, ΔH<40 kJ mol^{-1} the sorption process is a physisorption. Thus the obtained of −14.2 kJ mol^{-1} for ΔH the adsorption process was a physisorption [21]. The exothermicity of the adsorption process affirms the decrease in the adsorption capacity. The correlation coefficient was 0.996, which is a measure of how well the values concur with each other. The magnitude of correlation coefficient suggests that the obtained values of ΔH and ΔS are reliable. The adsorption process occurs between electrostatic interaction between the positively charged cobalt nanoparticles and the negatively charged CrO_4^{2-} ions.

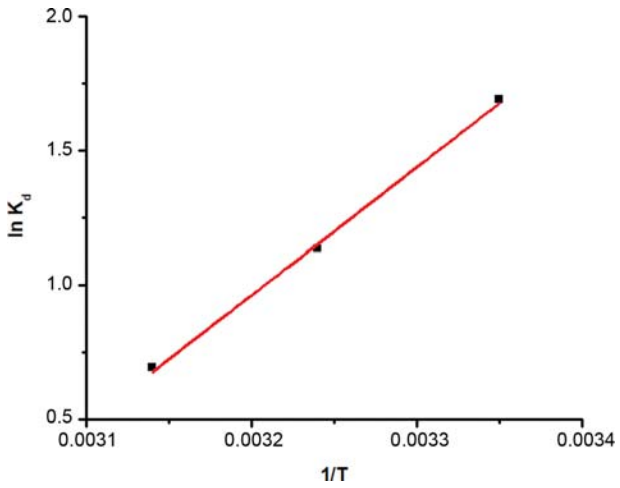

Fig. 14. The van't Hoff plot for the adsorption of Cr(VI) on Co-rGO.

3-3. Regeneration and Desorption

The economical feasibility of the Co-rGO is the ability of the composite to be regenerated. The Cr(VI) was soaked in an ethanol solution with 10% NaOH. The mixture was then ultrasoni-

Table 5. Table of thermodynamic parameters

T/K	ΔG/(kJ mol^{-1})	ΔH/(kJ mol^{-1})	ΔS/(kJ mol^{-1} K^{-1})
298	−1.72	−14.2	4.76
308	−1.95		
318	−2.21		

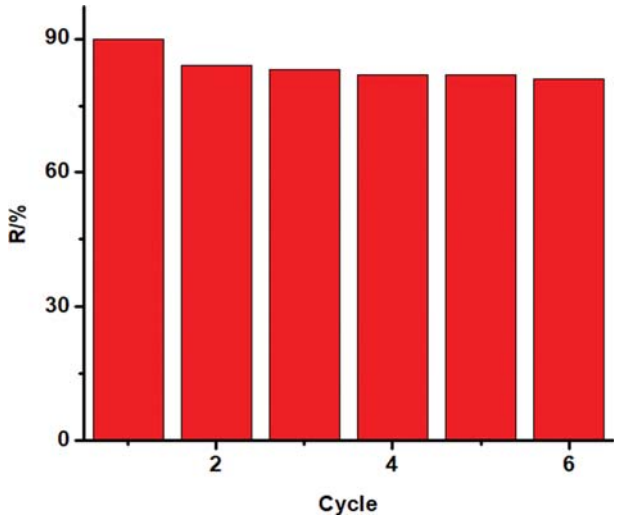

Fig. 15. The removal efficiency of recycled Co-rGO.

cated and loosened the electrostatic interaction between the Co-rGO and Cr(VI). Desorption was then achieved when CrO_4^{2-} was displaced by the OH^-. After the soaking and ultrasonication, the ethanol solution turned from a clear to a yellowish solution. The Co-rGO was separated from the solution by using a held magnet. The Co-rGO was washed with water and acetone. The Co-rGO was then dried in a vacuum oven at 60 °C. The concentration used for regeneration of Co-rGO was 20 mg L^{-1}. The adsorption-desorption cycles is shown in Fig. 15. The first regeneration resulted in a drop in the removal efficiency from 90% to 82%. The removal efficiency had not changed after sixth cycle.

CONCLUSIONS

The study was to synthesize Co-rGO using coprecipitation method, with graphene oxide and $Co(acac)_2$ as starting materials. The Co-rGO was characterized and found that the cobalt nanoparticles were on the surface of the rGO. The Co-rGO was a monocrystalline material. The Co-rGO was subsequently used in the removal of Cr(VI) under basic medium. High concentration of Cr(VI) saturates the active sites and decreases the removal efficiency of the Co-rGO. The adsorption processes follow pseudo-second-order kinetics. The best removal efficiency was at pH 8 which once exceeded, hydroxide ions competed with Cr(VI) ions for active adsorption sites. The adsorption fitted well to the Freundlich adsorption model over the Langmuir and Liu isotherm. The model suggested that the adsorption sites are heterogeneous. The adsorption process follows a monolayer to multilayer sorption with interaction between the adsorbed molecules. Adsorption process occurs between electrostatic interaction between the positively charge cobalt nanoparticles and the negatively charged CrO_4^{2-} ions. The adsorption capacity of the Co-rGO for Cr(VI) was 116 mg g^{-1}, which was higher than some of magnetic nanoparticles-graphene composites. The magnitude of the ΔH was 14.2 kJ mol^{-1} suggests that the adsorption process and the adsorption capacity decrease with increases temperature. The Co-rGO being a weak ferromagnetic material it was easily removed from Cr(VI) solution. The Co-rGO can be regenerated using an ethanol solution treated with 10% NaOH solution. The Co-rGO was recycled six times and showed no significant change in the removal efficiency.

ACKNOWLEDGEMENTS

This work is supported by the Department of Science and Technology (DST) through the National Research Foundation (NRF) Freestanding scholarship.

REFERENCES

1. M. F. Brigatti, G. Franchini, C. Lugli, I. Medici, L. Poppi and E. Turci, *Appl. Geochem.*, **15**, 1307 (2000).
2. L.-C. Hsu, S. L. Wang, Y. M. Tzou, C. F. Lin and J. H. Chen, *J. Hazard. Mater.*, **142**, 242 (2007).
3. S. R. Frois, M. T. Grassi and M. S. de Campos, *Anal. Methods*, **4**, 4389 (2012).
4. A. Nigam, S. Priya, P. Bajpai and S. Kumar, *Indian J. Med. Res.*, **139**, 349 (2014).
5. V. K. Gupta, M. Gupta and S. Sharma, *Water Res.*, **35**, 1125 (2001).
6. R. Dubey, J. Bajpai and A. K. Bajpai, *J. Water Process. Eng.*, **5**, 83 (2015).
7. A. K. Shanker, C. Cervantes, H. Loza-Tavera and S. Avudainayagam, *Environ. Int.*, **31**, 739 (2005).
8. M. Yusuf, F. M. Elfghi, S. A. Zaidi, E. C. Abdullah and M. A. Khan, *RSC. Adv.*, **5**, 50392 (2015).
9. A. Dabrowski, Z. Hubicki, P. Podkoscielny and E. Robens, *Chemosphere*, **56**, 91 (2004).
10. G. Ayoub, L. Semerjian, A. Acra, M. Fadel and B. Koopman, *J. Environ. Eng.*, **127**, 196 (2001).
11. M. M. Matlock, B. S. Howerton and D. A. Atwood, *Ind. Eng. Chem. Res.*, **41**, 1579 (2002).
12. Y. Zhang, L. Yan, W. Xu, X. Guo, L. Cui, L. Goa, Q. Wei and B. Du, *J. Mol. Liq.*, **191**, 177 (2014).
13. M. Soylak, Y. E. Unsal, N. Kizil and A. Aydin, *Food Chem. Toxicol.*, **2**, 517 (2010).
14. H. Saleem, M. Haneef and H. Y. Abbasi, *Mater. Chem. Phys.*, **204**, 1 (2018).
15. F. Halouane, Y. Oz, D. Meziane, A. Barras, J. Juraszek, S. K. Singh, S. Kurungot, P. K. Shaw, R. Sanyal, R. Boukherroub, A. Sanyal and S. Szinerits, *J. Colloid Interface Sci.*, **507**, 360 (2017).
16. H. Wang, X. Z. Yuan, Y. Wu, H. Huang, G. Zeng, Y. Liu, X. Wang, N. Lin and Y. Qi, *Appl. Surf. Sci.*, **279**, 432 (2013).
17. D. C. Marcano, D. V. Kosynkin, J. M. Berlin, A. Sinitskii, Z. Sum, A. Slesarev, L. B. Alemany, W. Lu and J. M. Tour, *ACS Nano*, **4**, 4806 (2010).
18. H. Wu, M. Shao, J. Gu and X. Wei, *Mater. Lett.*, **58**, 2166 (2004).
19. S. A. Salman, T. Usami, K. Kuroda and M. Okido, *J. Nanotechnol.*, **2014**, 1 (2014).
20. A. M. Prajapathi and M. K. Mondal, *Korean J. Chem. Eng.*, **36**, 1900 (2019).
21. D. R. Lima, A. Hosseini-Bandegharaei, P. S. Thue, E. C. Limam, Y. R. T. de Albequerque, G. S. dos Reis, C. S. Umpieries, S. L. P. Dias and H. N. Tran, *Colloids Surf. A*, **583**, 123966 (2019).
22. R. Muszynski, B. Seger and P. V. Kamat, *J. Phys. Chem. C. Lett.*, **112**,

5236 (2008).
23. J. Romero-González, J. R. Peralta-Videa, E. Rodríguez, S. L. Ramirez and J. L. Gardea-Torresdey, *J. Chem. Thermodyn.*, **37**, 343 (2005).
24. M. A. Al-Ghouti, M. A. M. Khraisheh, S. J. Allen and M. N. Ahmad, *J. Environ. Manage.*, **69**, 229 (2003).
25. J. M. Chaba and P. N. Nomngongo, *J. Water. Process Eng.*, **23**, 50 (2018).
26. H. T. Yang, Y. K. Sum, C. M. Shen, T. Z. Yang and H. J. Gao, *Surf. Interface Anal.*, **36**, 155 (2004).
27. I. R. Gonsalves and V. M. S. Verenkar, *J. Meth. Anal. Calorim.*, **108**, 877 (2012).
28. C.-S. Park, D. H. Kim, B. J. Shin, D. Y. Kim, H.-K. Lee and H.-S. Tae, *Materials*, **9**, 812 (2016).
29. X. Diez-Betru, S. Alvarz-Garcia, C. Botas, P. Alvarez, J. Sachez-Marcos, C. Prieto, R. Menendez and A. de Andres, *J. Mater. Chem. C*, **1**, 6905 (2013).
30. A. Al-Marri, M. Khan, M. Khan, S. F. Adil, A. Al-Wrthan, A. Z. Alkhathlan, W. Tremel, J. P. Labis, M. R. H. Siddiqul and M. N. Tahir, *Int. J. Mol. Sci.*, **16**, 1131 (2015).
31. S.-C. Kim, B. H. Kim, S.-J. Kim, Y.-S. Lee, H.-G. Kim, H. Lee, S. H. Park and S.-C. Jung, *J. Nanosci. Nanotechnol.*, **15**, 228 (2015).
32. P. R. Kumar, P. Kollu, C. Santhosh, K. E. V. Rao, D. K. Kim and A. N. Grace, *New J. Chem.*, **389**, 3654 (2014).
33. Z. Ji, X. Shen, G. Zhu, A. Zhou and A. Yuan, *J. Mater. Chem.*, **22**, 3471 (2012).
34. Y. Zhang, H.-L. Ma, J. Peng, M. Zhai and Z.-Z. Yu, *J. Mater. Sci.*, **48**, 1883 (2013).
35. J. Zhu, S. Wei, H. Gu, S. R. Rapole, Q. Wang, Z. Lou, N. Haldolaarachchige, D. P. Young and Z. Guo, *Environ. Sci. Technol.*, **46**, 977 (2012).
36. J. Hu and G. Chen, *Langmuir*, **24**, 11173 (2005).
37. A. Nafiey, A. Addad, B. Sieber, B. Chastanet, A. Barras, S. Szunerits and R. Boukherrrout, *Chem. Eng. J.*, **322**, 375 (2017).
38. X. Lv, X. Xue, G. Jiang, D. Wu, T. Sheng, H. Zhu and X. Xu, *J. Colloid Interface Sci.*, **417**, 51 (2014).
39. S. Yavari, N. M. Mahmodi, P. Teymouri, B. Shahmoradi and A. Maleki, *J. Taiwan Inst. Chem. E.*, **59**, 320 (2016).
40. S. Phanichphant, A. Nakaruk and D Channei, *Appl. Surf. Sci.*, **387**, 214 (2019).
41. L. Cui, X. Guo, Q. Wei, Y. Wang, L. Goa, L. Yan, T. Yan and B. Du, *J. Colloid Interface Sci.*, **439**, 112 (2015).
42. T. S. Kareen, M. Zubait, M. Duad, N. D. Mu'azu and M. A. Al-Harthi, *Korean J. Chem. Eng.*, **36**, 1057 (2019).
43. R. Lafi, A. Fradj, A. Hafiane and B. H. Hameed, *Korean J. Chem. Eng.*, **31**, 2198 (2014).
44. P. Wang, M. Cao, C. Wang, Y. Ao and J. H. J. Qian, *Appl. Surf. Sci.*, **290**, 119 (2014).
45. M. Song, Z. Duan, R. Qin, X. Xu, S. Lui, S. Song, M. Zhang, Y. Li and J. Shi, *Korean J. Chem. Eng.*, **36**, 869 (2019).
46. B. Babu and S. Gupta, *Adsorption*, **14**, 85 (2008).